Chemical Science

ROYAL SOCIETY OF CHEMISTRY

EDGE ARTICLE

View Article Online
View Journal | View Issue

Cite this: *Chem. Sci.*, 2025, **16**, 13847

All publication charges for this article have been paid for by the Royal Society of Chemistry

Received 6th May 2025
Accepted 23rd June 2025

DOI: 10.1039/d5sc03279b

rsc.li/chemical-science

Hydroxy-pendant tetrazole as the cage group for photoactivatable push–pull fluorophores†

Meng Li,[a] Maoting He[a] and Peng An *[ab]

Photoactivatable fluorophores enable selective fluorescence activation within a defined region of interest at a precisely controlled time point. This high degree of spatiotemporal control over fluorescence emission facilitates advanced imaging modalities and super-resolution microscopy techniques, allowing real-time monitoring of dynamic processes and nanoscale visualization of structural features. The development of photocage groups is the general and most popular strategy for designing photoactivatable fluorophores. Herein, we present hydroxy-pendant phenyl tetrazole as a novel photocage for push–pull photoactivatable fluorophores. Upon photolysis, this tetrazole-based photocage undergoes rapid cleavage with nitrogen extrusion, followed by nitrile imine-mediated nucleophilic addition and subsequent proton transfer to afford the corresponding hydrazone photoproduct. This tetrazole to hydrazone photoconversion leads to an electronic inversion from electron-withdrawing to electron-rich character, thereby triggering fluorescence turn-on *via* charge recombination. This phenyl tetrazole photocage was applicable in coumarin (Cou), nitrobenzoxadiazole (NBD), and naphthalimide (NP) fluorophores. The NP-based photoactivatable fluorophores enabled spatiotemporally resolved, targeted live-cell fluorescence imaging in both confocal and stimulated emission depletion (STED) microscopy, exhibiting rapid photoresponse, non-toxic byproduct release, bright fluorescence emission, and a high signal-to-background ratio.

Introduction

Photoactivatable fluorophores, showing turn-on fluorescence upon light irradiation, are valuable tools for tracking cellular dynamics, spatiotemporally controllable imaging, and super-resolution microscopy (SRM).[1] The general design strategy for photoactivatable fluorophores involves covalently conjugating the fluorophore with a photolabile caging (photocage) group to suppress its native fluorescence. Upon photoirradiation, controlled photochemical transformation of the photocage regenerates the active fluorophore, typically through either restoration of the original chromophore or conversion of the caging moiety to an auxochrome.[2] To date, numerous photocages have been developed, including the widely used *o*-nitrobenzyl and its derivatives,[3] diazoketone,[4] thiocarbonyl group,[5] azidophenyl moieties,[6] tetrazine,[7] oxime,[8] and 2,3-dihydro-1,4-oxathiine group,[9] each operating through distinct photochemical activation mechanisms. The predominant mechanism for photocage-mediated fluorescence activation relies on fluorescence quenching in the excited state through energy/electron transfer and subsequent restoration of emission occurring upon photolytic cleavage or structural transformation of the caging group. For example, the *o*-nitrobenzyl caging group can quench fluorophores through a photoinduced electron-transfer (PeT) process. Therefore, mono-2-nitrobenzyl-caged Tokyo-Green, displaying minimal fluorescence due to singlet excited-state quenching *via* PeT, exhibits substantial fluorescence enhancement by removal of the *o*-nitrobenzyl cage (Fig. 1a).[3b] Similarly, the 2,3-dihydro-1,4-oxathiine group induces fluorescence loss through an analogous PeT process. Following irradiation, fluorophore-generated singlet oxygen mediates oxidative conversion of the oxathiine moiety to its corresponding ester derivative, thereby terminating the PeT pathway and restoring fluorescence emission (Fig. 1b).[9] Moreover, tetrazine and oxime have been utilized as general fluorescence quenchers through distinct mechanisms: tetrazine derivatives quench *via* fluorescence resonance energy transfer (FRET) with the fluorophore, while oxime groups function by electronically attenuating the intrinsic charge transfer (ICT) process of the fluorophore (Fig. 1c and d).[7,8] An alternative fluorophore caging strategy employs photocage groups that structurally constrain fluorophores in their inactive forms.[4,10] This approach typically requires precise structural matching between the caging moiety and the target fluorophore. One representative implementation involves a diazoketone caged rhodamine fluorophore (Fig. 1e), where the caging group maintains rhodamine in a non-

[a]*School of Chemical Science and Technology Yunnan University, Kunming 650091, P. R. China. E-mail: anp@ynu.edu.cn*

[b]*Key Laboratory of Medicinal Chemistry for Natural Resource, Ministry of Education, Yunnan University, Kunming 650091, P. R. China*

† Electronic supplementary information (ESI) available. See DOI: https://doi.org/10.1039/d5sc03279b

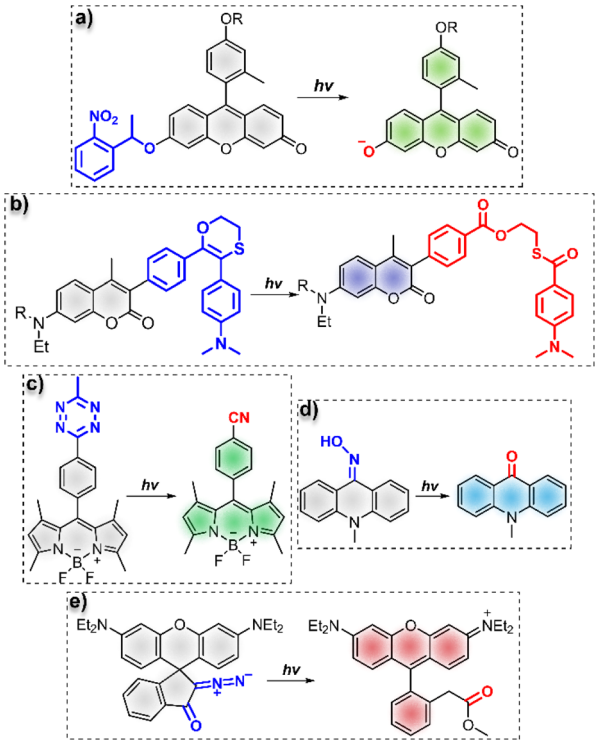

Fig. 1 Photoactivatable fluorophores with different types of photocage groups. (a) Photoactivatable fluorescein derivatives with a mono-2-nitrobenzyl-caged group. (b) 2,3-Dihydro-1,4-oxathiine-tagged photoactivatable coumarin fluorophore. (c) Tetrazine as a photocage to turn on the BODIPY fluorophore. (d) Oxime as a photocage for a 10-methylacridin-9(10*H*)-one fluorophore. (e) Photoactivatable 2-diazoketone caged rhodamine B.

fluorescent spirocyclic form until photolytic cleavage restores the fluorescent xanthene structure.[4] For most of the photocage groups, it takes from tens of minutes to hours for completion of the photouncaging reactions as monitored using UV-Vis/fluorescence spectra. Efficient photocages with rapid photolysis kinetics for real-time applications in dynamic biological systems are still highly desirable.

Herein, we present hydroxy-functionalized phenyl tetrazole as a general photocage for push–pull fluorophores, showing rapid photolysis kinetics. Tetrazoles represent an important class of nitrogen-rich heterocycles characterized by a five-membered ring structure comprising four nitrogen atoms and one carbon atom. In particular, aryl tetrazoles serve as photosensitive moieties that undergo rapid photolytic cleavage to generate a reactive nitrile imine (**NI**) intermediate with the extrusion of nitrogen.[11] In the presence of alkenes, these photogenerated **NI** dipoles participate in 1,3-dipolar cycloaddition with olefins to form the pyrazoline product.[12] This nitrile imine-mediated tetrazole-ene cycloaddition (NITEC) has found broad utility in biomolecular labelling and materials science.[13] Notably, the electrophilic character of **NI** intermediates enables additional reactivity pathways through nucleophilic addition reactions,[14] further expanding their versatility. We hypothesized that nitrile imine-mediated tetrazole-nucleophile addition (NITNA) could serve as an effective strategy for designing photoactivatable fluorophores based on three considerations: (i) 2,5-diaryl tetrazoles undergo rapid photolysis with clean release of benign nitrogen, (ii) the photoinduced NITNA reaction likely induces an electronic inversion character from electron-deficient tetrazole[15] to an electron-rich hydrazone product, and (iii) the electron donor–acceptor (D–A) type architecture represents conventional scaffolds employed in organic fluorophore design. Therefore, in the caged state, the phenyl tetrazole moiety, conjugated at the electron-donating terminus of D–A type fluorophores (**T-Flo**), disrupts the intrinsic push–pull electronic configuration. Upon irradiation, the photogenerated **NI** intermediate (**NI**) undergoes intramolecular nucleophilic addition with the pendant hydroxyl group, yielding a hydrazone derivative (**H-Flo**). This transformation leads to charge recombination to regenerate the electronic D–A structure, enabling significant fluorescence enhancement (Fig. 2a).

Results and discussion

Design, synthesis, and structures

To validate this hypothesis, we selected three representative push–pull fluorophore scaffolds: coumarin (Cou), nitrobenzoxadiazole (NBD), and naphthalimide (NP). Accordingly, we designed a series of diaryl tetrazole-based probes (**T-Cou**, **T-NBD**, and **T-NP**) featuring an *ortho*-hydroxymethylene substituent on the phenyl tetrazole cage to facilitate the formation of a favorable five-membered ring during the intramolecular nucleophilic addition (Fig. 2a and b). These probes were successfully synthesized through multistep organic transformations (Schemes S1–S3†). Upon photoirradiation, we anticipated that the tetrazoles would undergo photolytic cleavage to generate the **NI** intermediate while releasing nontoxic N_2, followed by intramolecular nucleophilic addition with the proximal hydroxyl group and subsequent proton transfer to yield the corresponding hydrazone products (Fig. 2c). To our delight, irradiation (310 nm, hand-held lamp, 9W) of the tetrazole precursors indeed afforded the expected hydrazone derivatives (**H-Cou**, **H-NBD**, and **H-NP**), which were unambiguously characterized by NMR and high-resolution mass spectrometry (HRMS). Details of the synthesis and characterization data are elaborated in the ESI (Schemes S1–S3 and Fig. S22–S27, S35–S40†).

Photophysical properties

To evaluate the suitability of *ortho*-hydroxy phenyl tetrazole as a general photocage for photoactivatable fluorophores, we then evaluated the photophysical properties of probes **T-Cou**, **T-NBD**, and **T-NP**. Significantly, the tetrazole-caged coumarin **T-Cou** demonstrated negligible fluorescence emission, with a remarkably low fluorescence quantum yield (FQY) below 0.1%. This substantial fluorescence quenching likely stems from effective disruption of the electron-donating feature of the amine through tetrazole attachment, thereby inhibiting the intrinsic intramolecular charge transfer (CT) process. The photoinduced chemical transformations were monitored using time-

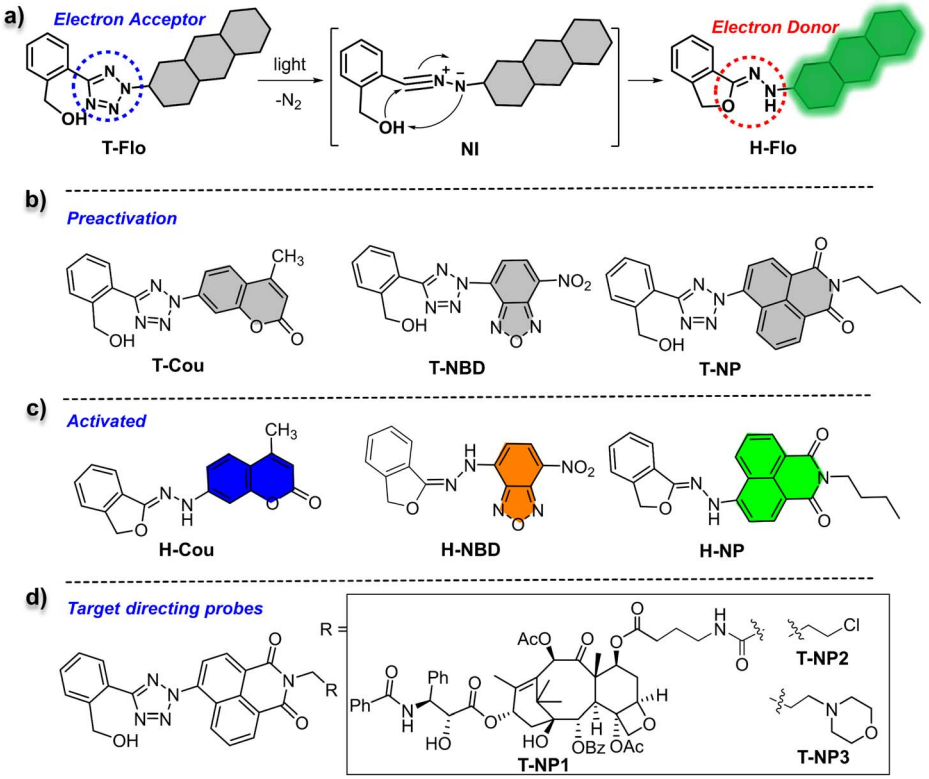

Fig. 2 Structures and reactions of hydroxy-tetrazole caged photoactivatable fluorophores. (a) Schematic of the design principle and reaction process of hydroxy-tetrazole caged photoactivatable fluorophores. (b) Structures of preactivated fluorophores **T-Cou**, **T-NBD**, and **T-NP**. (c) Structures of photoactivated fluorophores **H-Cou**, **H-NBD**, and **H-NP**. (d) Structures of microtubule-, endoplasmic reticulum (ER)-, and lysosome-targeting photoactivatable fluorophores.

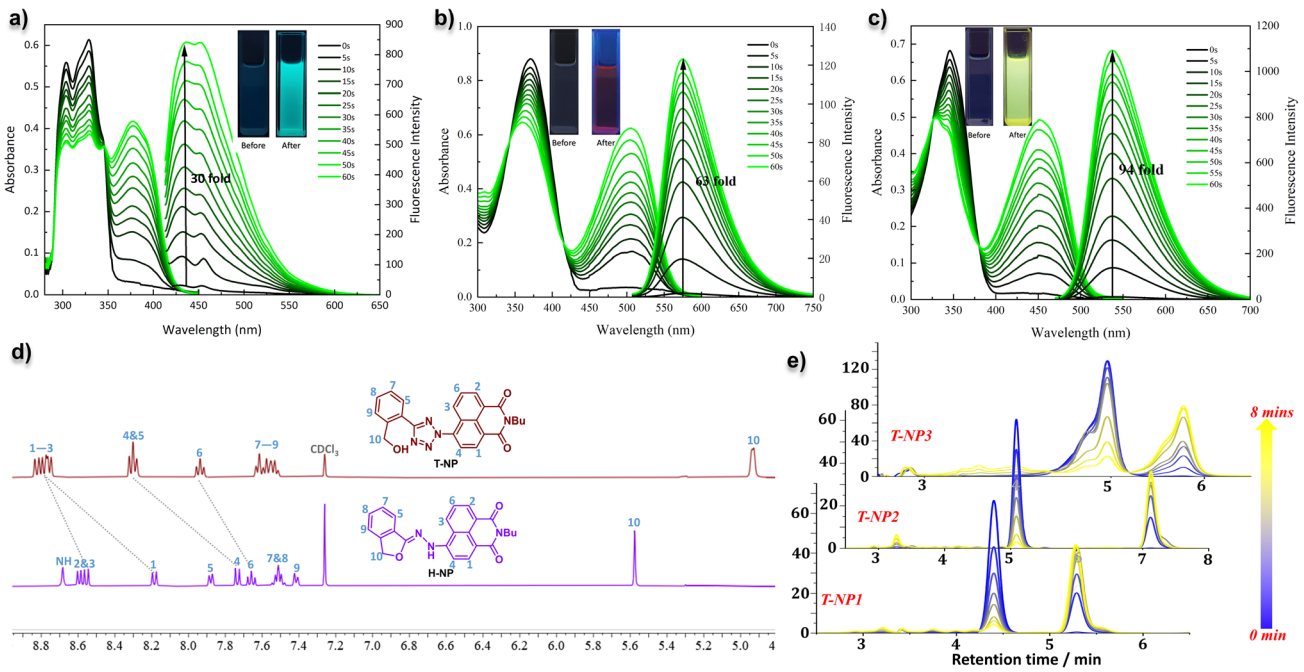

Fig. 3 (a–c) Changes in UV/Vis absorption and fluorescence emission spectra of **T-Cou** (a), **T-NBD** (b), and **T-NP** (c) upon UV irradiation (310 nm) at 10 μM. Inset: photographs of **T-Cou** (a), **T-NBD** (b), and **T-NP** (c) under 365 nm UV light before and after 1 min of irradiation. (d) ^{1}H NMR spectra of aromatic regions of preactivated fluorophore **T-NP** and photoactivated product **H-NP** (400 MHz, in $CDCl_3$). (e) Time-dependent HPLC traces of photoactivatable fluorescent probes **T-NP1**, **T-NP2**, and **T-NP3** upon 310 nm irradiation in THF for 0–8 mins.

Table 1 Photophysical properties of photoinduced products in solution[a]

	λ_{max} (nm)	ε_{max} (M^{-1} cm^{-1})	λ_{em} (nm)	Stokes shift (cm^{-1})	Φ_F
H-Cou	378	4.2×10^4	437/482[b]	1579	0.32/0.029[b]
H-NBD	505	4.2×10^4	574/595[c]	2380	0.014/0.007[c]
H-NP	451	4.9×10^4	537/560[c]	3550	0.44/0.072[c]

[a] Measured in THF (10 μM). [b] Measured in PBS (10 μM). [c] Measured in THF/PBS = 1 : 1 (10 μM).

dependent UV-Vis and fluorescence emission spectroscopy. The absorption spectrum of **T-Cou**, featuring primary maxima at 300 and 330 nm, gently decreased during illumination with 310 nm light over 60 s, concomitant with the emergence and rapid intensification of a new absorption band at ~375 nm (Fig. 3a). Fluorescence analysis demonstrated a substantial 30-fold enhancement at ~437 nm during only 1 of minute irradiation (30-fold, 10^{-5} M in THF, Table S1†). The spectral signatures are identical to those of the chemically synthesized **H-Cou** reference (Fig. S1†), confirming the formation of the anticipated hydrazone product. Compared to the non-emissive **T-Cou**, the photoactivation product **H-Cou** displayed significantly higher intensity of fluorescence with an FQY of 0.32 (Table 1). Similarly, both **T-NBD** and **T-NP** displayed analogous fluorescence turn-on profiles upon photoirradiation by forming hydrazone products (Fig. S2 and S3†), achieving remarkable 63-fold and 94-fold emission enhancements at 574 nm and 537 nm, respectively (Fig. 3b and c). The corresponding hydrazone products **H-NBD** (FQY = 0.014) and **H-NP** (FQY = 0.44) showed substantially improved quantum yields relative to their non-activated precursors **T-NBD** and **T-NP** (FQYs less than 0.1%).

To understand the electronic perturbation during the photouncaging process, we conducted ^{1}H NMR analyses and theoretical calculations. Taking **T-NP** to **H-NP** transformation as a representative example, the ^{1}H NMR signals revealed significant upfield shifts for aromatic protons in photoproduct **H-NP** compared to the caged precursor **T-NP** (Fig. 3d). Specifically, protons 1 and 4, in the benzene adjacent to the tetrazole ring, displayed a more pronounced shift of approximately 0.6 ppm than distal protons 2, 3, and 6. Analogous ^{1}H NMR perturbations were observed for the coumarin and NBD systems, which exhibit more pronounced upfield shifts of 1.2 ppm and 1.9 ppm for **H-Cou** and **H-NBD**, respectively compared to their tetrazole precursors (Fig. S5†). These consistent diamagnetic shifts unambiguously demonstrate an electronic inversion upon photoconversion, wherein the electron-withdrawing tetrazole moiety transforms into an electron-donating hydrazone group. This electronic switching effect regenerates the active push–pull configuration through charge recombination, resulting in increased emission.

We then conducted density functional theory (DFT) and time-dependent DFT (TD–DFT) calculations to further corroborate the push–pull electronic pattern of emitters **H-Cou**, **H-NBD**, and **H-NP**.

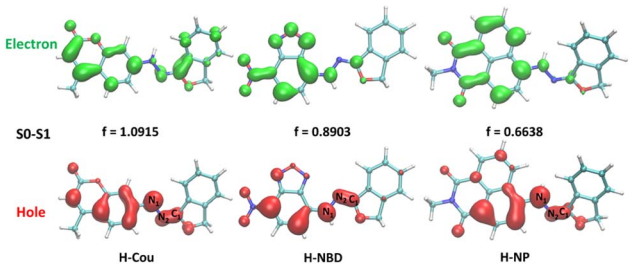

Fig. 4 Hole–electron surface analysis and oscillator strength *f* for the S_0–S_1 transition states of **H-Cou**, **H-NBD**, and **H-NP** based on TD–DFT calculations at the cam-b3lyp/def2-TZVP level of theory.

Geometry optimizations were performed at the CAM-b3lyp/def2-TZVP level of theory, and frequency analyses were used to verify these geometries as true minima on the potential energy surface. The TD–DFT calculations indicated that the ground state (S_0) to first excited state (S_1) excitations were mainly contributed by highest occupied molecular orbital (HOMO)–lowest unoccupied molecular orbital (LUMO) transitions in all three fluorophores, exhibiting substantial oscillator strengths ranging from 0.6638 to 1.0915 (Fig. 4 and S17†). The hole–electron analysis[16] for S_0–S_1 transitions demonstrated separated hole–electron surfaces, leading to significant internal charge transfer (ICT) from hydrazone (N1–N2–C1) to chromophore backbones in the first excited states (Fig. 4 and S20†), which did not appear in the caged tetrazole analogues (Fig. S19†). Moreover, the hole surface density was predominantly localized on diamine moieties and the *ortho*/*para* positions of the aniline rings, confirming the electron-donating nature of the photolytic hydrazone auxochromic group (Fig. 4). Meanwhile, the fluorophores **H-Cou**, **H-NBD**, and **H-NP** displayed bathochromic shifts and decreased emission efficiency in polar solvents, analogous to amine-based donor–acceptor (D–A) fluorophores (Fig. S9–S11†). This solvatochromic effect corroborates the push–pull nature of the fluorophores, which underwent polarity-dependent solvent–solute interactions arising from the formation of CT structures in the excited state.

Cellular fluorescence imaging

To demonstrate that the tetrazole-based photoactivatable fluorophores can be activated in live cells, we selected **T-NP** as the modelling prefluorophore and synthesized three biological probes **T-NP1**–**T-NP3**, for targeting specific biomacromolecules or organelles (Fig. 2d and Schemes S4, S5†) in live cells. In probe **T-NP1**, we employed paclitaxel, a well-known anticancer reagent, as the ligand because it would bind to abundant intracellular microtubules for fluorescence signal acquisition.[17] **T-NP2** and **T-NP3** with a chlorine and 2-morpholinoethylamine moiety were supposed to target endoplasmic reticulum (ER) and lysosome (Lyso), respectively.[18] Afterwards, the photoreactivity and emission properties of probes **T-NP1**–**T-NP3** were evaluated. The photochemical process was initially tracked by UV-Vis absorption spectroscopy. Upon irradiation (310 nm, hand-held lamp, 9W), **T-NP1**–**T-NP3** exhibited the formation of a characteristic hydrazone absorption band at ~460 nm, accompanied

by a slight decrease in absorbance at ~350 nm (Fig. S6–S8†). This spectral photoresponse is consistent with that observed for **T-NP** (Fig. 3c), indicating a similar photochemical transformation pathway.

Meanwhile, the high-performance liquid chromatography (HPLC) analyses suggested nearly clean photochemical conversions from tetrazoles to their photolytic products *in vitro* (Fig. 3e). As expected, non-fluorescent compounds **T-NP1**–**T-NP3** displayed rapid fluorescence turn-on (within 1–2 min) upon light irradiation, yielding fluorogenic products with FQYs of 0.46–0.55 in THF. The emission bands ($\lambda \approx 540$ nm) closely match that of **H-NP**, suggesting analogous fluorophore formation (Fig. S6–S8†). In response to polarity, a pronounced bathochromic shifted fluorescence emission (≈30 nm) in phosphate buffered saline (PBS) was observed for the generated fluorophores (Fig. S6–S8†).

We next evaluated the performance of these photoactivatable fluorophores in live-cell imaging. Cytotoxicity assessment revealed that **T-NP2** and **T-NP3** exhibited no cytotoxicity at concentrations up to 10 μM, while paclitaxel-conjugated derivative **T-NP1** induced a measurable reduction in cell viability (Fig. S12†). Therefore, HeLa cells were treated with 5 μM **T-NP1** for 45 min at 37 °C, washed with prewarmed PBS, and imaged *via* confocal fluorescence microscopy. Prior to photoactivation, no detectable fluorescence was observed inside the cells at the green channel of 500–600 nm ($\lambda_{ex} = 488$ nm), confirming the inactivity of the caged fluorophore. Following 310 nm light (hand-held lamp, 9W) irradiation, fluorescence in the cytoplasm appeared, and a 115-fold fluorescence enhancement was observed within 5 min of irradiation, attributed to the photochemical uncaging of phenyl tetrazole (Fig. 5a and S15a†). Quantitative analysis revealed a 65-fold signal-to-background ratio calculated from the mean cytoplasmic fluorescence intensity relative to background signals in the cell-free culture medium (Fig. S16a†). We subsequently investigated the turn-on ability of **T-NP2** for ER-specific imaging. HeLa cells incubated with 10 μM **T-NP2** probes for 3 h showed negligible fluorescence before activation. Following 310 nm light irradiation for 3.5 minutes, we observed a remarkable 122-fold fluorescence enhancement (Fig. 5b and S15b†) in the green channel (500–600 nm) with an exceptional signal-to-background ratio of 225 (Fig. 5b and S16b†). The intracellular fluorescence signals of the green channel from the activation of **T-NP2** overlapped well with those of co-incubated ER-Tracker Red ($\lambda_{em} = 615$ nm), suggesting the ER-targeted photoactivatable capability of **T-NP2**.

Photoactivatable fluorophores offer significant advantages for super-resolution microscopy techniques such as stimulated emission depletion (STED) imaging.[1i,19] We evaluated the lysosome-targeted probe **T-NP3** for STED imaging. Initial confocal microscopy studies indicated that a 108-fold fluorescence enhancement was observed in the **T-NP3**-incubated live cells upon 310 nm light irradiation (Fig. 6a, S15c and d†). The lysosomal specificity was validated through colocalization studies, where the generated fluorescence signals overlaid very well with the signals in the red channel of Lyso-Tracker Red DND-99 (Fig. 6a and S13†). For STED nanoscopy, HeLa cells were incubated with **T-NP3** at a 10 μM concentration for 3 h, followed by *in situ* photoactivation (310 nm, 6.0 min). Using 488 nm

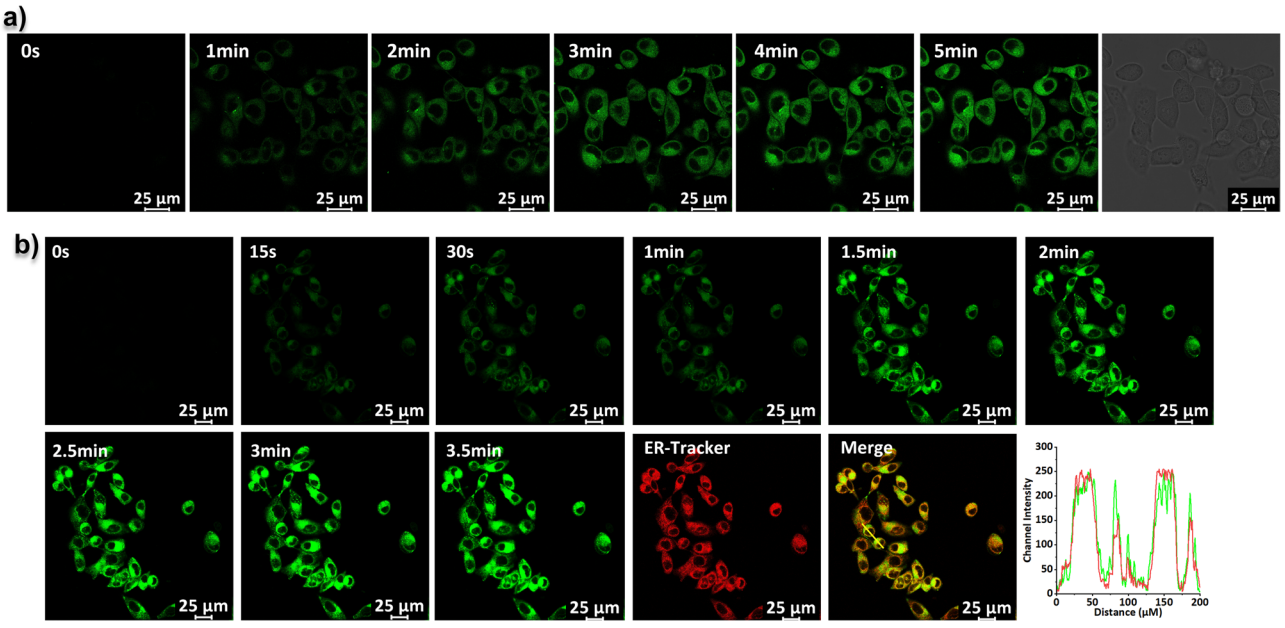

Fig. 5 (a) Time-course confocal micrographs of microtubule-targeting probe T-NP1 treated HeLa cells after photoillumination with 310 nm light. Ex = 488 nm. The cell culture was treated with a 5 μM concentration of the probe. The fluorescence was viewed in a 500–600 nm window as a green channel with differential-interference-contrast (DIC) microscopy. (b) Time-course confocal micrographs of ER-targeting probe T-NP2 treated HeLa cells after photoillumination with 310 nm light. Ex = 488 nm. The cell culture was treated with a 10 μM concentration of the probe. ER-Tracker Red was used as a marker (Ex = 570 nm). A plot of pixel fluorescence along the line in the merged photo is shown. The fluorescence was viewed in a 500–600 nm window for T-NP2 as a green channel and 610–740 nm window for ER-Tracker Red as a red channel.

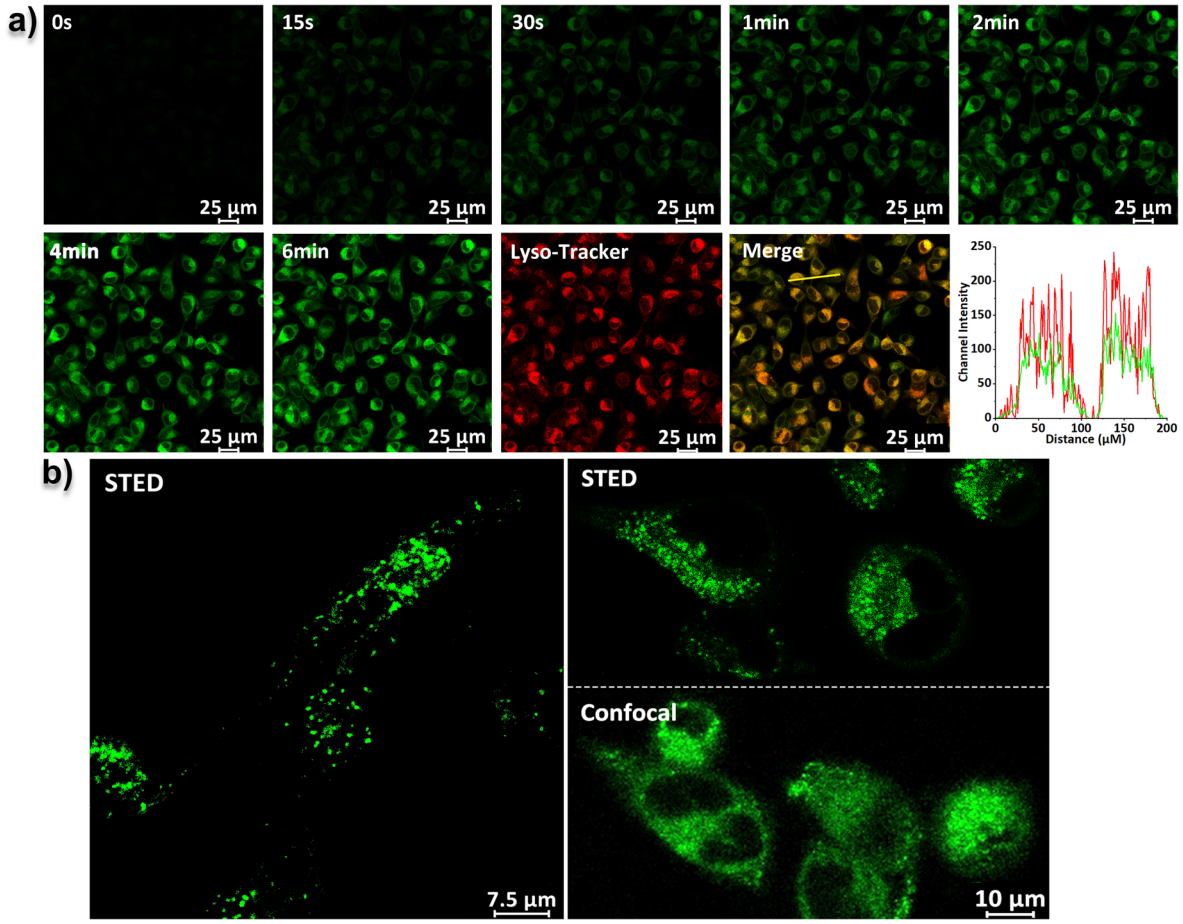

Fig. 6 (a) Time-course confocal micrographs of lysosome-targeting probe **T-NP3** treated HeLa cells after photoillumination with 310 nm light. Ex = 488 nm. The cell culture was treated with a 10 μM concentration of the probe. Lyso-Tracker Red was used as a marker (Ex = 570 nm). A plot of pixel fluorescence along the line in the merged photo is shown. The fluorescence was viewed in a 500–600 nm window for **T-NP3** as a green channel and 610–740 nm window for Lyso-Tracker Red as a red channel. (b) Confocal and STED images of lysosomes in living HeLa cells incubated with **T-NP3** (10 μM) after 310 nm light activation and 488 nm and 660 nm as excitation and STED light, respectively.

excitation coupled with a 660 nm STED beam, we successfully achieved super-resolved imaging of lysosomal structures (Fig. 6b). The resulting images revealed distinct lysosomal morphology at sub-diffraction resolution, clearly resolving their characteristic dense-precipitated organization (Fig. S14†).

Conclusions

In this work, we developed hydroxy-pendent phenyl tetrazole as a new type of photocage for photoactivatable fluorophores. The mechanism of fluorescence turn-on is based on the recovery of intramolecular charge transfer (ICT) of the push–pull fluorophores. Strategically, the inactive fluorophores, with the electron-deficient phenyl tetrazole attached at the electron-donor site, undergo photoinduced tetrazole photolytic cleavage, followed by nucleophilic addition of free hydroxy to nitrile imine intermediates generate the active form of fluorophores by charge recombination of electron "push–pull" structures. The electron-structure reversal was proved using the ^{1}H NMR spectrum and DFT calculations. This strategy is applicable for coumarin, nitrobenzoxadiazole, and naphthalimide and the photoactivation characteristics were demonstrated by both ensemble spectral measurements and target-directing fluorescence imaging in live cells. Notably, the naphthalimide-based lysosome-targeting probe, which can tolerate STED pulses at 660 nm, was applied to STED imaging to visualize lysosomes in live cells. Theoretically, using this hydroxy-pendant phenyl tetrazole photocage is supposed to be a general strategy for constructing more push–pull type photoactivatable fluorophores.

Data availability

The full experimental details, synthetic procedures, characterization data, UV-Vis, fluorescence, and NMR spectra, computational details, and fluorescence imaging associated with this article are provided in the ESI.†

Author contributions

M. Li performed the major synthesis work, property studies, and biological imaging. M. He helped with synthesis, photophysical property measurements, and cell cultures. P. An

conceived the concept and performed the DFT calculations. M. Li and P. An prepared the manuscript. All the authors analyzed and interpreted the results.

Conflicts of interest

There are no conflicts to declare.

Acknowledgements

We are grateful for the financial support provided by the National Natural Science Foundation of China (22461046 and 22061046), Yunnan Fundamental Research Projects (202501AS070062 and 202401AT070475), and the project of the Innovative Research Team of Yunnan Province (202405AS350010). We thank the Advanced Analysis and Measurement Center of Yunnan University for assistance with instrumentation.

Notes and references

1 (*a*) Z. Zhou, Z. Luo, X. Xu, S. Yang, Z. Qing, J. Liu and R. Yang, *Trends Anal. Chem.*, 2020, **125**, 115811; (*b*) T. J. Chozinski, L. A. Gagnon and J. C. Vaughan, *FEBS Lett.*, 2014, **588**, 3603–3612; (*c*) L. Zhou, X. Zhang, Y. Lv, C. Yang, D. Lu, Y. Wu, Z. Chen, Q. Liu and W. Tan, *Anal. Chem.*, 2015, **87**, 5626–5631; (*d*) J. B. Grimm, T. Klein, B. G. Kopek, G. Shtengel, H. F. Hess, M. Sauer and L. D. Lavis, *Angew. Chem., Int. Ed.*, 2016, **55**, 1723–1727; (*e*) Y. Zhang, K.-H. Song, S. Tang, L. Ravelo, J. Cusido, C. Sun, H. F. Zhang and F. M. Raymo, *J. Am. Chem. Soc.*, 2018, **140**, 12741–12745; (*f*) Y. Zhang, Y. Zheng, A. Tomassini, A. K. Singh and F. M. Raymo, *ACS Appl. Opt. Mater.*, 2023, **1**, 640–651; (*g*) S. Hauke, A. von Appen, T. Quidwai, J. Ries and R. Wombacher, *Chem. Sci.*, 2017, **8**, 559–566; (*h*) R. Lin, M. L. Bossi, M. Remmel, E. D'Este, A. N. Butkevich and S. W. Hell, *Nat. Chem.*, 2022, **14**, 1013–1020; (*i*) M. Weber, T. A. Khan, L. J. Patalag, M. Bossi, M. Leutenegger, V. N. Belov and S. W. Hell, *Chem.–Eur. J.*, 2021, **27**, 451–458; (*j*) M. Xiao, Y.-K. Zhang, R. Li, S. Li, D. Wang and P. An, *Chem.–Asian J.*, 2022, **17**, e202200634; (*k*) Y.-K. Zhang, M. Li, L. Ruan and P. An, *Chem. Commun.*, 2022, **58**, 10404–10407; (*l*) H. Kashima, M. Kamiya, F. Obata, R. Kojima, S. Nakano, M. Miura and Y. Urano, *Chem. Commun.*, 2021, **57**, 5802–5805; (*m*) A. N. Butkevich, M. Weber, A. C. Cereceda Delgado, L. M. Ostersehlt, E. D'Este and S. W. Hell, *J. Am. Chem. Soc.*, 2021, **143**, 18388–18393.

2 (*a*) P. Klán, T. Šolomek, C. G. Bochet, A. Blanc, R. Givens, M. Rubina, V. Popik, A. Kostikov and J. Wirz, *Chem. Rev.*, 2013, **113**, 119–191; (*b*) P. Wang, *Asian J. Org. Chem.*, 2013, **2**, 452–464; (*c*) C. Brieke, F. Rohrbach, A. Gottschalk, G. Mayer and A. Heckel, *Angew. Chem., Int. Ed.*, 2012, **51**, 8446–8476.

3 (*a*) W.-H. Li and G. Zheng, *Photochem. Photobiol. Sci.*, 2012, **11**, 460–471; (*b*) T. Kobayashi, Y. Urano, M. Kamiya, T. Ueno, H. Kojima and T. Nagano, *J. Am. Chem. Soc.*, 2007, **129**, 6696–6697; (*c*) G. A. Krafft, W. R. Sutton and R. T. Cummings, *J. Am. Chem. Soc.*, 1988, **110**, 301–303.

4 (*a*) V. N. Belov, C. A. Wurm, V. P. Boyarskiy, S. Jakobs and S. W. Hell, *Angew. Chem., Int. Ed.*, 2010, **49**, 3520–3523; (*b*) V. N. Belov, G. Y. Mitronova, M. L. Bossi, V. P. Boyarskiy, E. Hebisch, C. Geisler, K. Kolmakov, C. A. Wurm, K. I. Willig and S. W. Hell, *Chem.–Eur. J.*, 2014, **20**, 13162–13173; (*c*) J. B. Grimm, B. P English, H. Choi, A. K Muthusamy, B. P Mehl, P. Dong, T. A Brown, J. Lippincott-Schwartz, Z. Liu, T. Lionnet and L. D Lavis, *Nat. Methods*, 2016, **13**, 985–988.

5 J. Tang, M. A. Robichaux, K.-L. Wu, J. Pei, N. T. Nguyen, Y. Zhou, T. G. Wensel and H. Xiao, *J. Am. Chem. Soc.*, 2019, **141**, 14699–14706.

6 (*a*) S. J. Lord, N. R. Conley, H.-l. D. Lee, R. Samuel, N. Liu, R. J. Twieg and W. E. Moerner, *J. Am. Chem. Soc.*, 2008, **130**, 9204–9205; (*b*) S. J. Lord, H.-l. D. Lee, R. Samuel, R. Weber, N. Liu, N. R. Conley, M. A. Thompson, R. J. Twieg and W. E. Moerner, *J. Phys. Chem. B*, 2010, **114**, 14157–14167.

7 A. Loredo, J. Tang, L. Wang, K.-L. Wu, Z. Peng and H. Xiao, *Chem. Sci.*, 2020, **11**, 4410–4415.

8 L. Wang, S. Wang, J. Tang, V. B. Espinoza, A. Loredo, Z. Tian, R. B. Weisman and H. Xiao, *Chem. Sci.*, 2021, **12**, 15572–15580.

9 X. Zhang, D. Guan, Y. Liu, J. Liu, K. Sun, S. Chen, Y. Zhang, B. Zhao, T. Zhai, Y. Zhang, F. Li and Q. Liu, *Angew. Chem., Int. Ed.*, 2022, **61**, e202211767.

10 (*a*) M. S. Frei, P. Hoess, M. Lampe, B. Nijmeijer, M. Kueblbeck, J. Ellenberg, H. Wadepohl, J. Ries, S. Pitsch, L. Reymond and K. Johnsson, *Nat. Commun.*, 2019, **10**, 4580; (*b*) J. Folling, V. Belov, R. Kunetsky, R. Medda, A. Schonle, A. Egner, C. Eggeling, M. Bossi and S. W. Hell, *Angew. Chem., Int. Ed.*, 2007, **46**, 6266–6270; (*c*) J. C. Vaughan, G. T. Dempsey, E. Sun and X. Zhuang, *J. Am. Chem. Soc.*, 2013, **135**, 1197–1200; (*d*) G. T. Dempsey, M. Bates, W. E. Kowtoniuk, D. R. Liu, R. Y. Tsien and X. Zhuang, *J. Am. Chem. Soc.*, 2009, **131**, 18192–18193.

11 (*a*) P. Scheiner and W. M. Litchman, *J. Chem. Soc., Chem. Commun.*, 1972, 781–782; (*b*) S.-L. Zheng, Y. Wang, Z. Yu, Q. Lin and P. Coppens, *J. Am. Chem. Soc.*, 2009, **131**, 18036–18037; (*c*) L. M. T. Frija, M. L. S. Cristiano, A. Gomez-Zavaglia, I. Reva and R. Fausto, *J. Photochem. Photobiol. C: Photochem. Rev.*, 2014, **18**, 71–90; (*d*) S. Flesch and P. Vöhringer, *Angew. Chem., Int. Ed.*, 2007, **61**, e202205803.

12 (*a*) R. Huisgen, M. Seidel, G. Wallbillich and H. Knupfer, *Tetrahedron*, 1962, **17**, 3–19; (*b*) Y. Wang, C. I. Rivera Vera and Q. Lin, *Org. Lett.*, 2007, **9**, 4155–4158.

13 (*a*) G. S. Kumar and Q. Lin, *Chem. Rev.*, 2021, **121**, 6991–7031; (*b*) W. Song, Y. Wang, J. Qu and Q. Lin, *J. Am. Chem. Soc.*, 2008, **130**, 9654–9655; (*c*) P. An, Z. Yu and Q. Lin, *Chem. Commun.*, 2013, **49**, 9920–9922; (*d*) J. Li, L. Huang, X. Xiao, Y. Chen, X. Wang, Z. Zhou, C. Zhang and Y. Zhang, *J. Am. Chem. Soc.*, 2016, **138**, 15943–15949; (*e*) Y. Wu, G. Guo, J. Zheng, D. Xing and T. Zhang, *ACS Sens.*, 2019, **4**, 44–51; (*f*) C. Rodriguez-Emmenegger, C. M. Preuss, B. Yameen,

O. Pop-Georgievski, M. Bachmann, J. O. Mueller, M. Bruns, A. S. Goldmann, M. Bastmeyer and C. Barner-Kowollik, *Adv. Mater.*, 2013, **25**, 6123–6127; (*g*) L. Rieger, B. Pfeuffer and H.-A. Wagenknecht, *RSC Chem. Biol.*, 2023, **4**, 1037–1042; (*h*) J. O. Mueller, D. Voll, F. G. Schmidt, G. Delaittre and C. Barner-Kowollik, *Chem. Commun.*, 2014, **50**, 15681–15684; (*i*) C. J. Durr, P. Lederhose, L. Hlalele, D. Abt, A. Kaiser, S. Brandau and C. Barner-Kowollik, *Macromolecules*, 2013, **46**, 5915–5923; (*j*) C. Wang, M. M. Zieger, A. Schenzel, M. Wegener, J. Willenbacher, C. Barner-Kowollik and C. N. Bowman, *Adv. Funct. Mater.*, 2017, **27**, 1605317; (*k*) V. X. Truong, J. O. Holloway and C. Barner-Kowollik, *Chem. Sci.*, 2022, **13**, 13280–13290; (*l*) S. Wijker, R. Monnink, L. Rijnders, L. Deng and A. R. A. Palmans, *Chem. Commun.*, 2023, **59**, 5407–5410.

14 (*a*) Z. Li, L. Qian, L. Li, J. C. Bernhammer, H. V. Huynh, J.-S. Lee and S. Q. Yao, *Angew. Chem., Int. Ed.*, 2016, **55**, 2002–2006; (*b*) P. An, T. M. Lewandowski, T. G. Erbay, P. Liu and Q. Lin, *J. Am. Chem. Soc.*, 2018, **140**, 4860–4868; (*c*) W. Konrad, C. Fengler, S. Putwa and C. Barner-Kowollik, *Angew. Chem., Int. Ed.*, 2019, **58**, 7133–7137.

15 C. Leonhardt, A. Mauri, I. Garin, N. W. Rosemann, W. Wenzel, U. Lemmer, M. Kozlowska and S. Bräse, *Chem.–Eur. J.*, 2024, **30**, e202401682.

16 (*a*) T. Lu and F. Chen, *J. Comput. Chem.*, 2012, **33**, 580–592; (*b*) Z. Liu, T. Lu and Q. Chen, *Carbon*, 2020, **165**, 461–467.

17 (*a*) A. Desai and T. J. Mitchison, *Annu. Rev. Cell Dev. Biol.*, 1997, **13**, 83–117; (*b*) V. Bevilacqua, M. King, M. Chaumontet, M. Nothisen, S. Gabillet, D. Buisson, C. Puente, A. Wagner and F. Taran, *Angew. Chem., Int. Ed.*, 2014, **53**, 5872–5876.

18 (*a*) W. Xu, Z. Zeng, J.-H. Jiang, Y.-T. Chang and L. Yuan, *Angew. Chem., Int. Ed.*, 2016, **55**, 13658–13699; (*b*) D. Singh, D. Rajput and S. Kanvah, *Chem. Commun.*, 2022, **58**, 2413–2429.

19 J. G. Danzl, S. C. Sidenstein, C. Gregor, N. T. Urban, P. Ilgen, S. Jakobs and S. W. Hell, *Nat. Photon.*, 2016, **10**, 122–128.